AIAA 2007-184

45th AIAA Aerospace Sciences Meeting and Exhibit, 8-11 Jan 2007, Reno, Nevada

Air Plasma Actuators for Effective Flow Control

Subrata Roy[*], K.P. Singh[†]

Computational Plasma Dynamics Laboratory and Test Facility
Mechanical and Aerospace Engineering, University of Florida
Gainesville, FL 32611-6300, USA

Datta V. Gaitonde[‡]

Computational Sciences Branch
Air Force Research Laboratory
Wright Pat AFB, Ohio 45433, USA

An asymmetric dielectric barrier discharge model is presented for real gas eight species air chemistry using a self-consistent multi-body system of plasma, dielectric and neutral gas modeled together to predict the electrodynamic momentum imparted to the working gas. The equations governing the motion of charged and neutral species are solved with Poisson equation on finite elements using a Galerkin *weak* formulation. Two specific geometries were used. First the unsteady electrodynamic force development mechanism is studied over a flat plate due to charge and neutral species production from adjacent air-like N_2/O_2 mixtures in a radio frequency driven barrier discharge. The solutions show a dominance of O^- and N_2^+ ions. The time average of the streamwise force shows mostly acceleration above the actuator but a small decelerating force downstream of the powered electrode inducing a fluctuation in the temporal evolution of streamwise velocity. This decelerating component needs further investigation as this may inherently limit the performance of a dbd plasma actuator. The computed electron temperature based on the electric field resembles the visible glow that is commonly reported in the literature. In another case, neutral gas flow is considered over a 5 deg conical crosssection for demonstration of active control using pulsed direct current and dielectric barrier discharges. The results demonstrate the need for utilization of multiple actuators for controlling a largely separated flow.

Nomenclature

D	Diffusion coefficient, cm^2/s	O	Oxygen atom
E	Electric field, V/cm	O_2^+	Positive oxygen ion
E	Electron charge, coulomb	O^-	Negative oxygen ion
ε	Permittivity, farad/m	ω	Applied frequency, radians
F	Electric force density, dynes/cm^3, $\mu N/cm^3$	P	Pressure, Pa
ϕ	Potential, V	T	Time coordinate, s
K	Rate coefficients, $cm^3 s^{-1}$	T	Temperature, eV
k_B	Boltzmann constant	**V**	Velocity, m/s
L	Electrode length, cm	X	Spatial coordinate, cm
λ_D	Electron Debye length, cm		
M	mass, kg		
μ	Mobility, $cm^2V^{-1}s^{-1}$	Subscripts:	
N	Number density, cm^{-3}	α	Species
N_2	Nitrogen molecule	B	Boltzmann
N	Nitrogen atom	E	Electron, finite element
N_2^+	Positive nitrogen ion	I	Ion
O_2	Oxygen molecule	N	Neutral

I. Introduction

ELECTRODYNAMIC modifications of air flowing around flat plates and air craft wings have been documented both experimentally and numerically.[1-3] These are primarily surface barrier discharges using asymmetric configurations

[*] Associate Professor of Mechanical Engineering, 336 MAE-B, PO Box 116300, and AIAA Associate Fellow.
[†] Post Doctoral Research Associate of the CPDL, AIAA Senior Member.
[‡] Technical Area Leader, Air Vehicles Directorate/VAAC, 2210 8th St., and AIAA Associate Fellow.

of electrode sets. The symmetric configuration of electrode sets can produce flow oscillation similar to synthetic jets. For plasma actuators with spatially displaced electrodes the airflow inducement is close to the dielectric surface with a time-averaged flow velocity measured between 1-3 m/s. These actuators exhibit several benefits in active flow control applications, including absence of moving parts, rapid on-off deployment and attractive self-limiting characteristics. The discharge may be characterized as transient with a time scale of the order of a few microseconds while that for the bulk gas flow is in milliseconds. This allows the fluid to respond relatively instantaneously to the electrical inputs. Experimental study and numerical predictions on the effect of different discharge parameters such as applied voltage waveform, distance between electrodes, dielectric thickness and permittivity are documented by various researchers.[4-5] These results show the volumetric body force increases as a function of frequency and applied voltage. The parametric relationship is not clear and is an area of continued investigation. Also the nature of the plasma gas interaction is not well understood. Acoustic measurements of the dielectric barrier discharge (DBD) plasma actuator[6] suggest that compressibility effects may contribute in the momentum coupling between plasma and neutral gas. Specific modality of discharge whether it is glow, Townsend or streamers will help determine how the body force is transported from charge to neutral species. The effect of this body force in controlling three dimensional laminar and transitional flow structures that have been studied utilizing both phenomenological and first-principles models.

Phenomenological and circuit based models have shown some success in mimicking overall electrical characteristic of the discharge but are fundamentally limited from inherent static and/or predetermined charge imposition.[7] The first principle models suitable for capturing detailed dynamics are also computationally challenging. For example, the surface barrier discharge in these actuators consists of repeated burst of micro-discharges which appears as an optical glow due to nanosecond timescales. Resolution of a typical micro-discharge driven by electron decay requires running simulation at a timescale of picoseconds or lower, thus imposes practical restriction to ever reaching the fluid timescale which is in milliseconds. Recent development of a loosely coupled fluid plasma formulation[5,8] has shown reasonable success in describing radio frequency (rf) powered electro-hydro-dynamic (EHD) control of NACA wing stall, laminar separation over a ramp, boundary layer transition on a flat plate, and turbulent separation over a wall-mounted hump. The plasma equations are based on a self-consistent simulation of charge species continuity and electric field equations. Once the reasonable periodicity is achieved in plasma characteristic, the temporally resolved EHD force is employed into the fluid equations to predict the effect of plasma in flow actuation. Interestingly, for moderate Reynolds numbers either co-flow or counter-flow pulsed actuators with sufficiently high frequency (kHz) were found to mitigate wing stall.[9] Unsteady flow actuation with a duty factor seemed to perform better than continuous operation of the rf plasma actuator. These results underscore the importance of accurately resolving the unsteady body force and understanding its transition and turbulence enhancement mechanisms for effective plasma actuation.

Numerical simulations of an asymmetrically arranged dbd actuator employing multispecies hydrodynamics[5] and Monte-Carlo (PIC-DSMC) methods[10] by independent research groups have found that ionization is not equal during positive and negative part of the alternating cycle producing a net force in one direction. Recently, the dc corona discharges and ac dielectric barrier discharges have been investigated under a range of operating conditions. Adjustment of the actuator geometry, dielectric materials, power frequency and RMS voltage show improvement in power transferred to the neutral gas flow by ion-neutral collisions. Also power losses due to inadequate impedance matching of the power supply to the actuator, dielectric heating, and power required to maintain the atmospheric pressure plasma have been reduced for better performance of actuator.[4]

In our earlier work, we have shown that electron deposition downstream of the overlap region of the electrodes results in formation of virtual negative electrode which always attracts the ions. The force on the charge separation is in the positive-x direction during most of the positive half of the rf voltage and in negative-x direction during most of negative half of the rf voltage. The magnitude of the former force is higher that the latter. Thus, domain integration of the force on the charge separation and time average of the force was found primarily to be in the positive-x and negative-y direction. We solved the equations governing dynamics of electrons, ions and fluid to obtain spatio-temporal profiles of electron density, ion density, electric potential, neutral gas density and neutral gas velocity. We documented how the EHD force is controlled by the dielectric characteristics, applied voltage, frequency and the asymmetric configuration of the electrodes, thickness of the exposed electrode. Additionally, we utilized the force field calculated from the first principles[5] to predict the effect of increasing number of electrodes on the wall jet while the electrodes are kept at a single phase and at a phase gap. The momentum transfer to the gas was also predicted for varying the distance between the powered electrodes.

Recently we have presented a real gas model with air-like N_2/O_2 mixture and have shown preliminary results predicting the effect of voltage in EHD force generation for eight species air chemistry.[11] In this paper we summarize our recent developments with the atmospheric barrier discharge model for eight species of air-like medium and the generated EHD force interactions over a flat dielectric. We also present pulsed dc and rf based surface discharge models for control of separated gas flow about a conical cross-section. This paper is organized as follows. Section II describes the problem statement for air chemistry and computed results. Section III describes and interprets the flow control simulation about the conical surface. Section IV summarizes the conclusions.

II. Air Chemistry in Plasma Actuator

Fig. 1 shows schematic of an asymmetric single dielectric barrier plasma actuator. It consists of two electrodes separated by a dielectric. The upper electrode is exposed to the air while the lower electrode is placed underneath the dielectric. The region simulated is 4 cm long and 1 cm high. The lower part of the domain consists of a 0.1 cm thick insulator with dielectric constant $\varepsilon_d = 10\varepsilon_0$ for diamond while the upper part is filled with air of $\varepsilon_f = 1.0055\varepsilon_0$, where ε_0 is permittivity of the free space. We have assumed negligible thickness for electrodes. The powered electrode extends from x=1.7 cm to x=1.9 cm at y=0.1 cm, the grounded electrode is from 2.1 cm to 2.3 cm at y=0, with a 0.2 cm gap between electrodes along the x-axis. The embedded electrode is grounded and an alternating voltage of $\phi = 1500\sin(10000\pi t)$ volts is applied to the exposed electrode.

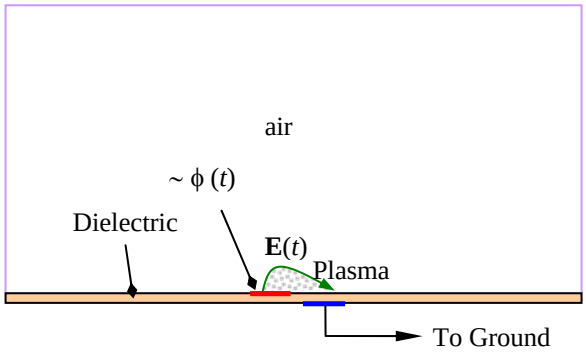

FIG. 1. Schematic of asymmetric single dielectric barrier plasma actuators operating in air.

For the air chemistry we neglect the metastable species along with N^{4+} and O^{4+} due to their extremely fast recombination rates. Also, the numerical complexity is further simplified by excluding nitrous oxide at this stage. The model equations governing chemistry of discharge are as follows.[12]

(1) Nitrogen model

(a) Ionization $e + N_2 \rightarrow N_2^+ + 2e$, (1a)

(b) Dissociation $e + N_2 \rightarrow 2N + e$, (1b)

(c) Dissociative recombination $e + N_2^+ \rightarrow N_2$, (1c)

(2) Oxygen model

(a) Ionization $e + O_2 \rightarrow O_2^+ + 2e$, (2a)

(b) Dissociation $e + O_2 \rightarrow 2O + e$, (2b)

(c) Dissociative attachment $e + O_2 \rightarrow O_- + O$, (2c)

(d) Recombination $O^- + O_2^+ \rightarrow O + O_2$, (2d)

(e) Dissociative recombination $O + O^- \rightarrow O_2 + e$, (2e)

The drift-diffusion form of continuity and Poisson equations for the electrons, ions and neutrals are as follows:

$$\frac{\partial n_e}{\partial t} + \nabla.(n_e \mathbf{v}_e) = k_1 n_e n_{N_2} - k_3 n_e n_{N_2^+} + (k_5 - k_7) n_e n_{O_2} + k_9 n_e n_{O_2^+}, \quad (3)$$

$$\frac{\partial n_N}{\partial t} + \nabla.(n_N \mathbf{v}_N) = 2k_2 n_e n_{N_2}, \quad (4)$$

$$\frac{\partial n_{N_2}}{\partial t} + \nabla.(n_{N_2} \mathbf{v}_{N_2}) = -k_1 n_e n_{N_2} - k_2 n_e n_{N_2} + k_3 n_e n_{N_2^+} \quad (5)$$

$$\frac{\partial n_{N_2^+}}{\partial t} + \nabla.(n_{N_2^+} \mathbf{v}_{N_2^+}) = k_1 n_e n_{N_2} - k_3 n_e n_{N_2^+} \quad (6)$$

$$\frac{\partial n_{O_2}}{\partial t} + \nabla.(n_{O_2} \mathbf{v}_{O_2}) = -(k_4 + k_5 + k_6) n_{O_2} n_e + k_7 n_{O^-} n_{O_2^+} + k_8 n_e n_{O_2^+} \quad (7)$$

$$\frac{\partial n_O}{\partial t} + \nabla.(n_O \mathbf{v}_O) = (2k_5 + k_6) n_e n_{O_2} + k_7 n_{O^-} n_{O_2^+} \quad (8)$$

$$\frac{\partial n_{O^-}}{\partial t} + \nabla.(n_{O^-} \mathbf{v}_{O_-}) = k_6 n_e n_{O_2} - k_7 n_{O^-} n_{O_2^+} \quad (9)$$

$$\frac{\partial n_{O_2^+}}{\partial t} + \nabla.(n_{O_2^+} \mathbf{v}_{O_2^+}) = k_4 n_e n_{O_2} - k_7 n_{O^-} n_{O_2^+} - k_8 n_e n_{O_2^+} \quad (10)$$

$$\nabla \bullet (\varepsilon \nabla \phi) = 4\pi e (n_e + n_{O^-} - n_{n_2^+} - n_{O_2^+}), \quad (11)$$

with momentum flux $n_\alpha \mathbf{v}_\alpha = -\mathrm{sgn}(e) n_\alpha \mu_\alpha \nabla\phi - D_\alpha \nabla n_\alpha$, and electric field $\mathbf{E} = -\nabla\phi$.

The electron temperature is calculated from $\mathbf{E} = k_B T_e/(\nabla n_e/n_e)$, which is obtained assuming an initial Boltzmann distribution, $n_e \propto \exp(e\phi/k_B T_e)$. Various rate coefficients k_1, k_2,…k_8 related to in Eqs. (1a) through (2e) are obtained from Kossyi et al.[12] as functions of electron temperature. The secondary electron emission from the exposed surface is taken as a function of incident electron energy[13] and remains small, i.e., less than 10^{-3}. No material sputtering of the surface is considered. The current balance is maintained at the surface. In Eqns. (3)-(11), n_α and $\mathbf{v}_\alpha$ are density and velocities of species α. The mobilities μ_α and diffusion rates D_α are taken from Ellis et al.[14]. The bulk density of the air is taken to be 1.3 kg/m^3. Atmospheric ratio of 3.6 is taken for nitrogen to oxygen gas molecules. The self-consistent formulation is solved using a Galerkin variational formulation based finite-element method[5] to obtain electron, ion and neutral species densities of nitrogen and oxygen, and the electric potential.

Initial and boundary conditions are as follows. The all initial particle concentrations, except those of the electrons, nitrogen and oxygen molecules, are taken to be zero. Initial oxygen molecule density is taken as 10^{24}/m^3 and the electron density is taken as 10^4/m^3. Initial rf potential is also zero. All neutral particle concentrations are taken zero at the boundaries of the dielectric and normal components of flux are zero at outer boundaries of plasma. Normal components of electric field are taken zero on all the outer boundaries of the domain (dielectric as well as plasma domain). No electron and ion current flow inside the dielectric is considered. Electric field normal to the dielectric surface is discontinuous by the separated charge.

The simulation results at the quasi-periodic 40th cycle are given in Figures 2-11. Figure 2 plots the temporal average of the O_2^+ ions in the domain. The time average was calculated by taking an average of the computed nodewise distributed data from 21 equally spaced time stations in a 2π cycle. A peak of 2×10^{13} ions is observed very close to surface over the grounded electrode. The exposed electrode accumulates an average of 1.5×10^{13} ions /m^3. The density decreases sharply by two orders of magnitude. The thickness of this patch is within a few microns indicating a thin sheath layer (~λ_D). Corresponding positive nitrogen ions N_2^+ in figure 3 show a high concentration (3×10^{14} ions/m^3) very close to the electrodes. Interestingly, the negative oxygen atom production shown in figure 4 is of the same level of that of positive nitrogen molecules. Obviously, the negative oxygen atom plays a dominant role in oxygen chemistry.

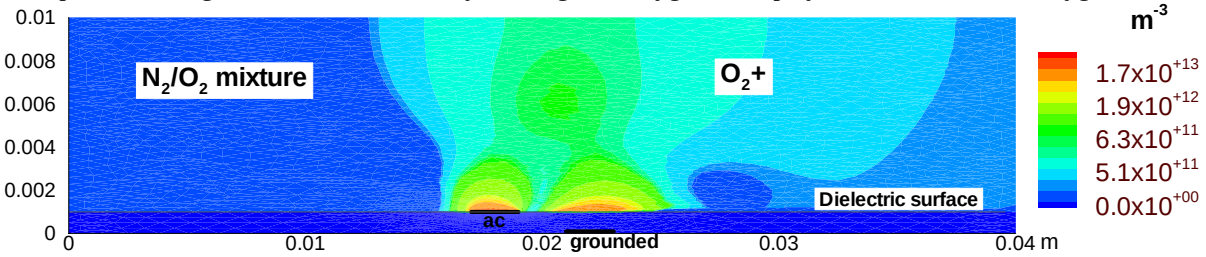

Figure 2: Distribution of positive oxygen ions shows a very thin sheath layer about the electrodes.

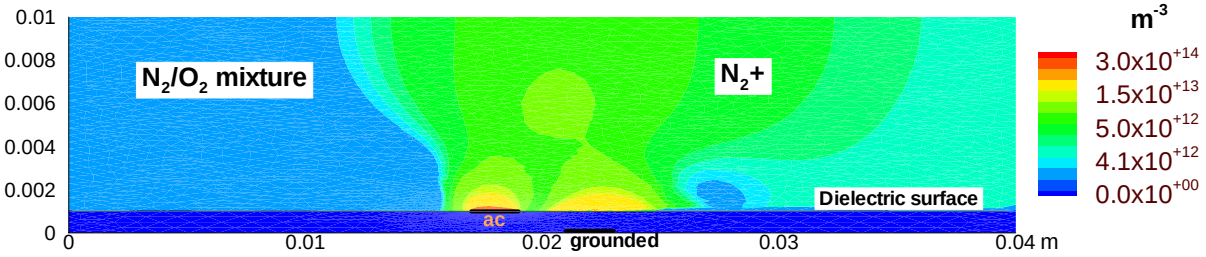

Figure 3: Contours show the time average production of nitrogen ions.

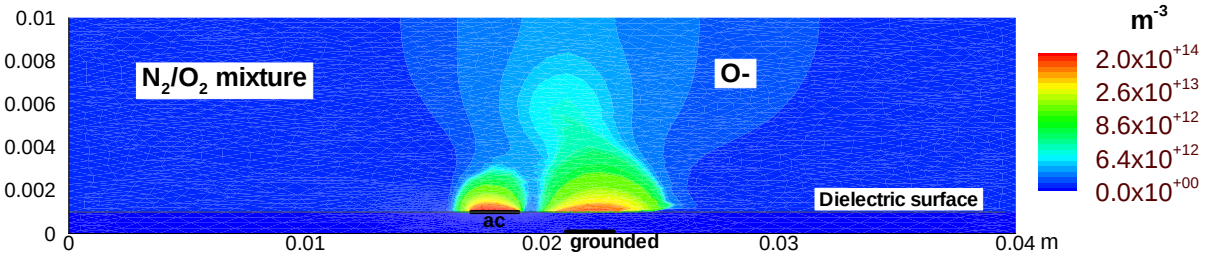

Figure 4: Distribution of negative oxygen atoms shows production of ions about a very thin sheath (~λ_D) layer.

While the nitrogen and oxygen ions are concentrated in the sheath region about the electrodes, the neutral nitrogen and oxygen atom production shown in figures 5 and 6, respectively, follows the electric field. The highest density of these neutral atoms is near the corner of the exposed electrode and between the two electrodes. The oxygen atom number density is four times (2×10^{14} /m^3) than that of the nitrogen atoms. Figure 7 plots the distribution of time averaged space charge density ($n_{N_2^+} + n_{O_2^+} - n_{O^-} - n_e$) of the computational domain. Clearly there is a 2mm thick cloud of net positive charge of 10^{13} /m^3 above the exposed electrode with a Debye length (λ_D) thick negative layer attached to the right corner. The top of the grounded electrode is covered with a cloud of negative charge of peak density 3.4×10^{12} /m^3. This is reflective of a DC-offset that should be experimentally validated (see e.g, Fig. 10 of Font et al.[10]).

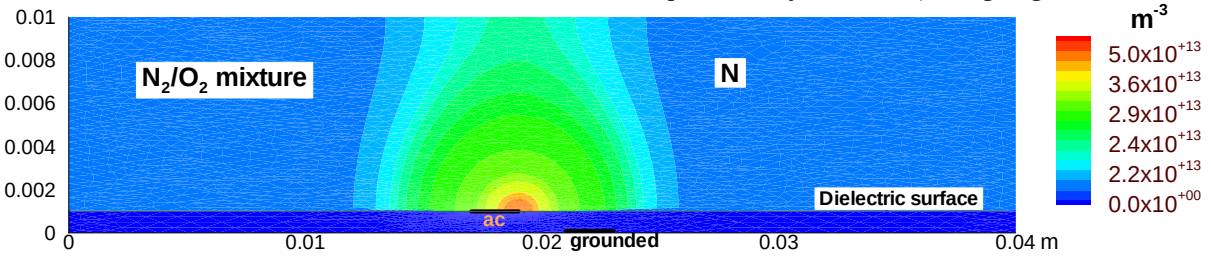

Figure 5: Time average of nitrogen atoms above show peak just downstream of the exposed electrode.

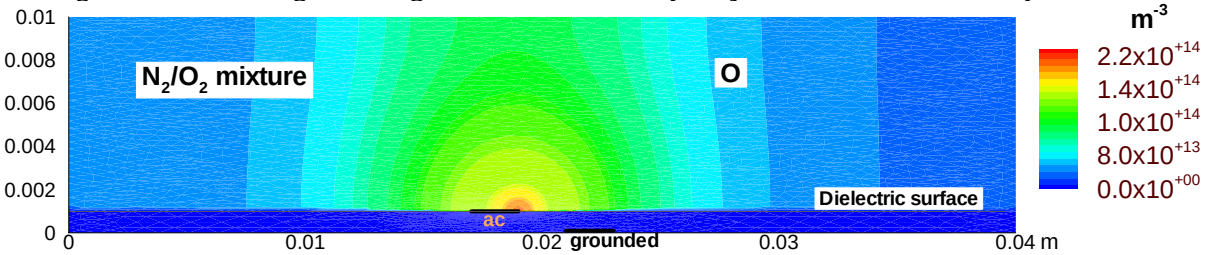

Figure 6: Time average of oxygen atom production above show peak just downstream of the exposed electrode is nearly four times than that of nitrogen.

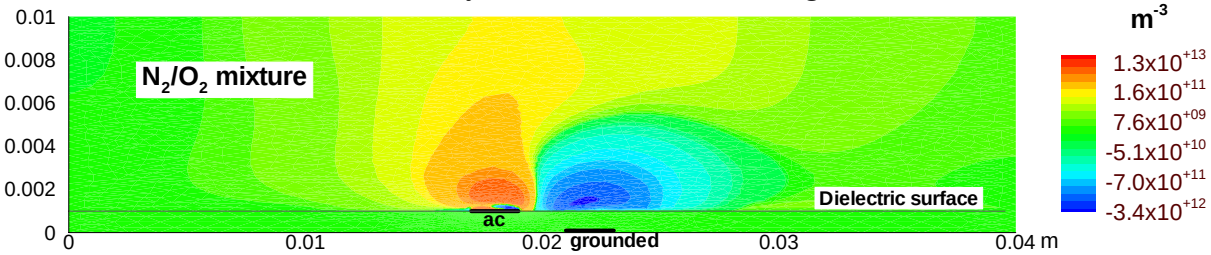

Figure 7: Time average of space charge density shows net accumulation of positive and negative charge.

The spatial variations of positive nitrogen and oxygen ions along 10 x-locations are described in Figures 8 (a) and 8 (b), respectively. The locations are selected from 1mm upstream of the exposed electrode (x=16mm) to 2mm downstream of the grounded electrode (x=25mm). At nearly .5mm above the midpoint of the exposed electrode, both positive ions show a peak. Here again, confirming the observation of Figures 2 and 3, the nitrogen positive ions show an order of magnitude higher number density than the oxygen counterpart. The sheath structure is clearly visible in both figures 8 (a) and 8 (b). Figure 9 plots the time evolution of the charge distribution at 11 stations equally spaced in a 2π cycle. The selected x-location in this case is at the right corner of the exposed electrode (x=19mm). As mentioned before, the oxygen chemistry is largely dominated by the negative atoms that can be clearly observed comparing figures

9 (a) and 9 (b). The net space charge density ($n_{N_2^+} + n_{O_2^+} - n_{O^-} - n_e$) due to the species chemistry considered is shown in figure 9 (c). While it appears that the line curve looks symmetric, a close observation reveals a slightly negative bias (~10^{13} /m^3) during the cycle. The streamwise (x) component of the time averaged electrodynamic volume force $e(n_{N_2^+} + n_{O_2^+} - n_{O^-} - n_e)E_x$ as presented in figure 10 shows that over the majority of the actuator, over the exposed and part of the grounded electrodes, the force is positive and will push the bulk air in the forward direction. Downstream of this, however, there is a negative force resisting the acceleration of the flow. While the accelerating force is about 2100 N/m^3, the decelerating force is only a fraction (-600 N/m^3). In the experiment this may be reflected as a dip in the ever increasing velocity curve as time evolves though a cycle. We believe this deceleration present in any dbd actuator inherently limits the performance and needs to be carefully explored.

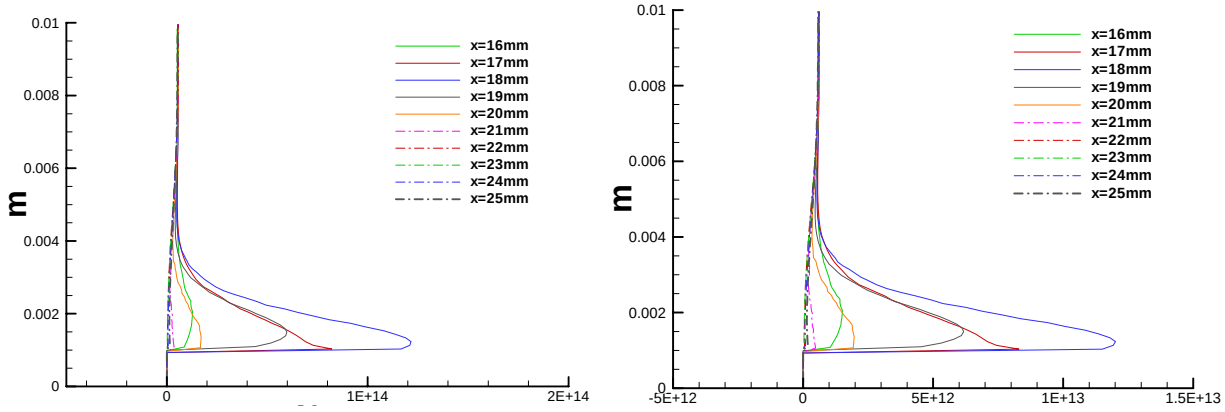

(a) Population of N_2^+ (b) Population of O_2^+

Figure 8: The distribution of positive ions away from the surface at 2π/5.

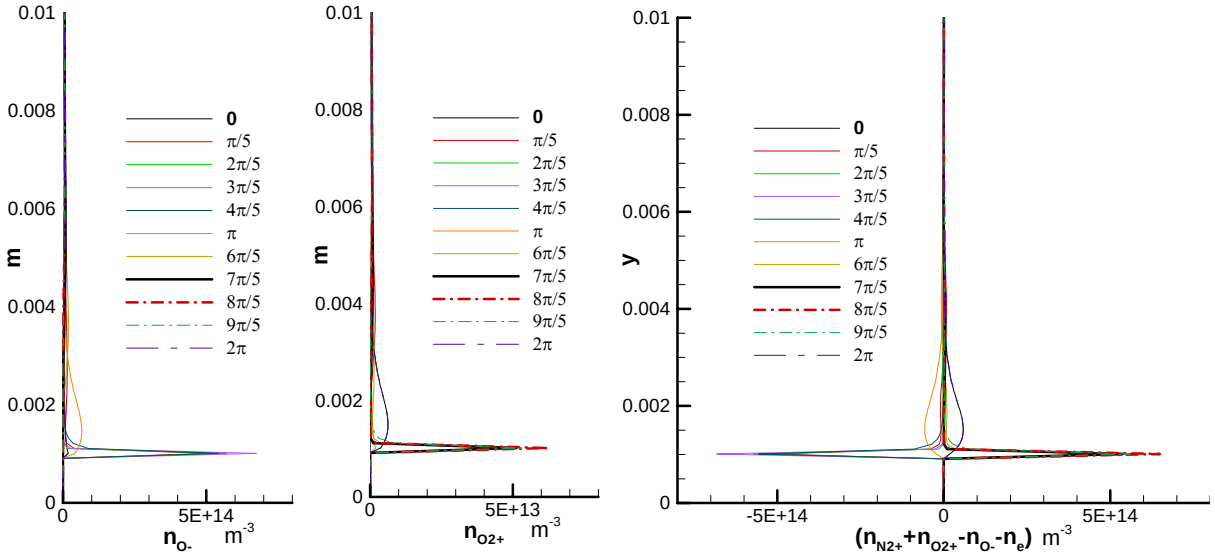

Figure 9: Time evolution of positive and negative oxygen ions and the space charge density at x=19mm.

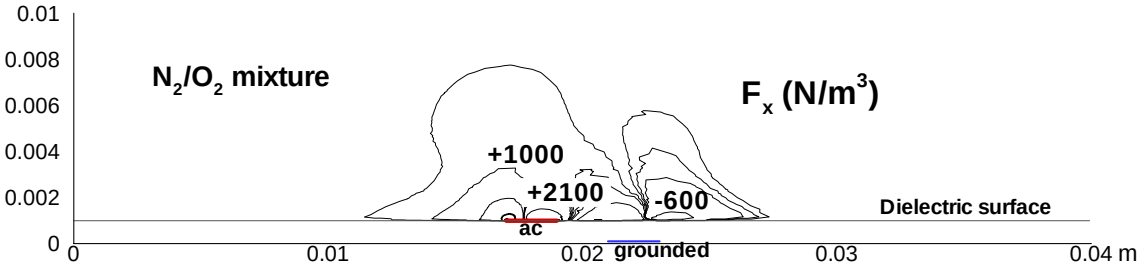

Figure 10: Time average of streamwise EHD force distribution based on air chemistry at the 40th cycle.

The distribution of computed electron temperature above the dielectric surface is plotted in figure 11. It shows the region of high temperature at the edge of the exposed electrode extended towards the grounded electrode. This is important as the visible optical glow will coincide with this temperature validating the experiments.[1,2] The peak electron temperature is about 2.2 eV just at the corner of the powered electrode resembling the highest electric field in that region.

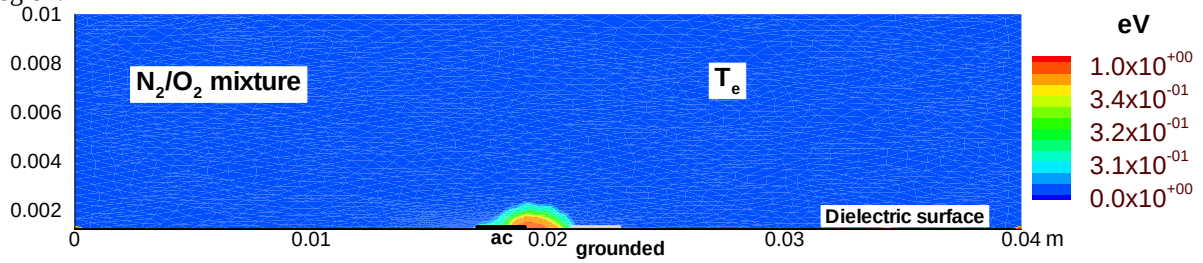

Figure 11: Distribution of electron temperature above the dielectric surface shows the peak temperature (2.2 eV) is just downstream of the exposed electrode.

III. Separated Flow Control about a Conical Cross-section

Schematic of flow control on a fore-body of an aircraft using plasma discharge plasma with an incident gas flow angle α is shown in figure 12a. The geometry is obtained from Ref. 15. Width of the domain is 2 meter and height is 1 meter. Gas is incident at an angle α with 10 m/s velocity. Angle at the nose of the forebody is 5^o. We have studied two geometries, one with dielectric barrier discharge plasma actuator and another with seven pairs of electrodes powered with pulsed dc voltage. Thickness of electrodes is assumed infinitesimally small for both the geometries. Following is description of the geometry with dielectric barrier discharge plasma actuator. Dielectric is located from x=1.2 m to x=1.21 m with dielectric thickness equal to 1.0 mm. The rf electrode is located at x=1.203 m to x=1.204 m at y=0.301 m. Grounded electrode is x=1.206 m to x=1.207 m at y=0.3 m. The electrodes for pulsed dc geometry are located at y=0.3 m from x=1.05 to 1.172. Length of each electrode is 2 mm and distance between electrodes is 8 mm. There are seven pairs of electrodes. Each pair is powered by a pulsed dc potential.

Initial electron and ion densities are $10^9/m^3$. Initial voltage is zero. A 10 m/s neutral gas flow is imposed at the left boundary with an angle of attack of $\alpha = 15°$ (17.5° with the centerline of the forebody). Initial air density is 1.2 Kg/m^3 and initial gas temperature is 300 K**.** Boundary conditions for Poisson's equation are as follows: potential $\phi = \phi_0 \sin(50000\pi t)$ with $\phi_0 = 500$ volts for DBD case and $\phi = \phi_0 \sin^{20}(1000\pi t)$, with $\phi_0 = 1200$ volts for pulsed dc voltage case. The potential is applied to the first electrode of the pair for pulsed dc case. Other electrodes of each pair are grounded. Electric insulation condition (normal component of electric field equal to zero) is assumed at outer boundaries of the domain and at the surface of forebody. Following are boundary conditions related to electrons and ions continuity equations: the currents flow normal only to the electrodes because it is a equipotential surface. Homogeneous Neumann conditions are applied to the outer edges of the domain and electric insulation is assumed at the surface of forebody. The currents flow normal as well as parallel to the dielectric surface. The boundary conditions for Navier-Stokes equations are as follows: The no-slip condition (u=0 and v=0) is assumed for the gas neutrals at the surface of forebody, dielectric surface (for dielectric barrier discharge case) and at electrodes. The velocity at the left boundary of upper domain is set equal to u=9.65 m/s and v=2.58 m/s. Neutral boundary conditions are applied to the outer edges of the domain. The self-consistent formulation is solved using a Galerkin variational formulation based finite-element method to obtain electron and ion density, electric potential, neutral velocity, density and gas temperature.

Figure 12 (b) shows streamlines and vectors of gas velocity at the end of 0.1 sec without any plasma discharge obtained by solving Navier-Stokes equations. We can see a recirculation bubble near the nose of the forebody. These kinds of separation bubbles are harmful to the performance of the aircraft. An rf voltage for DBD or a pulsed dc voltage is switched on after 0.1 second to see the effect. Figure 12 (c) shows profile of pulsed dc voltage as a function of time. The results of Figure 13 are for dielectric barrier discharge after 25 cycles of plasma discharge activity and that of Figures 14 for pulsed dc plasma discharge after 10 cycles of plasma discharge activity.

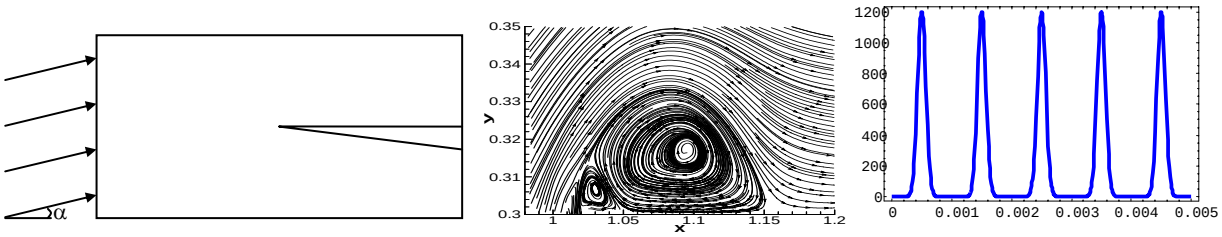

(a) **(b)** **(c)**

Figure 12: (a) Schematic of the conical section, (b) separated flow at 17.5 deg AOA, (c) DC pulsed at 1 kHz rate.

Figure 13 shows effect of Dielectric Barrier Discharge (DBD) plasma actuator on flow control on a forebody of an aircraft. We do not solve temperature equations (3) for the results of this figure. After 0.1 second rf voltage $\phi = 500 \sin(2\pi ft)$ volts and f = 25 kHz, is switched on to see the effect. Figure 13 (a) shows vectors of time averaged electrodynamic force $e(n_i - n_e)\mathbf{E}$. It can be seen from the figure that force is directed in forward direction which may help in elimination of recirculation. Figure 13 (b) shows streamlines and vectors of gas velocity after 25 cycles of rf discharge activity. We can see that recirculation is affected by DBD plasma actuator; however, flow is not attached to the surface all over the surface of forebody. This is because single dielectric barrier plasma actuator is not sufficient to cover the entire length of recirculation and recirculation is not eliminated. Multiple dielectric barrier discharge plasma actuators on the surface of forebody may control vortex dynamics of the flow. We suggest multiple pair of electrodes powered with pulsed dc potential as an alternative to multiple DBD plasma actuators in this paper.

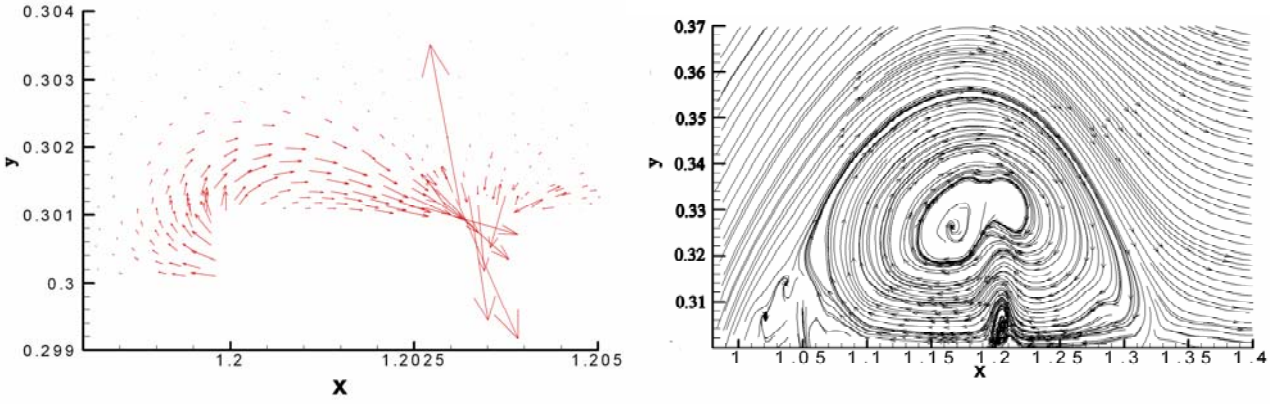

(a) **(b)**

Figure 13: (a) Time averaged EHD force vectors shows force distribution about the DBD actuator, and (b) Gas flow streamtraces after 50 cycles of barrier discharge. (x and y are in meters)

Figure 14 shows the effect of plasma discharge on flow control about a the crosssection of a conical forebody due to electrodynamic force only. We want to see the effect played by electrodynamic force on flow control on a forebody. Figure 14 (a) shows charge separation and vectors of electrodynamic force at the peak of the spike. At its peak the EHD force vectors are directed mostly downwards which helps in destruction of the big recirculation bubble and formation of small bubbles. Figure 14 (b) shows streamlines and vectors of gas velocity after 10 cycles of plasma discharge activity by a pulsed dc potential. We can see that effect of plasma discharge on recirculation is highest in this case and a big recirculation bubble is destroyed and small bubbles are formed. These small bubbles may not be that much harmful to the performance of the aircraft as a big bubble.

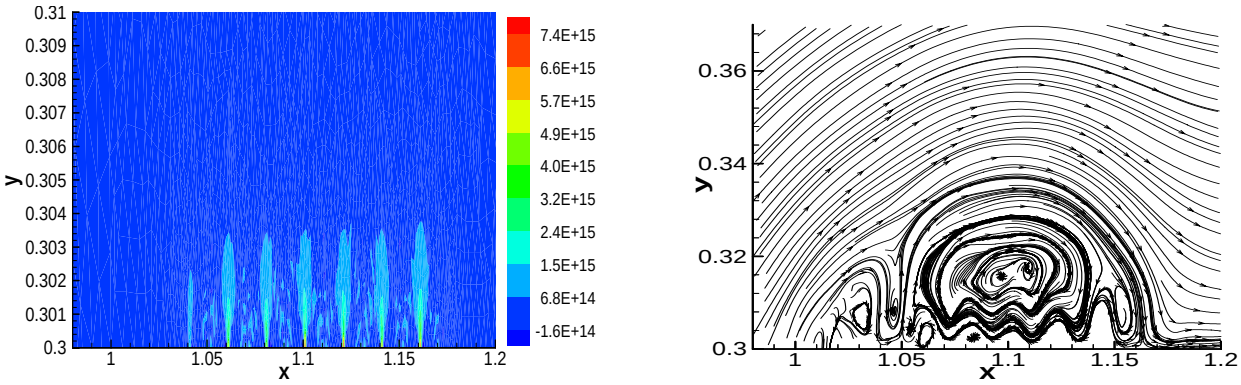

(a) **(b)**

Figure 14: (a) Space charge distribution at the peak of pulsed dc, (b) Streamtraces show the effect of EHD force on flow structure.

IV. Conclusions

We have utilized a finite element based formulation to model the air chemistry around a plasma actuator and numerically compared the capability of a set of pulsed dc and a single dbd actuator to control largely separated flow about a forebody conical cross-section. The N_2/O_2 air chemistry consists of eight charged and neutral species and demonstrated the dominance of N_2^+ and O^- ions. The time average of the streamwise force shows mostly acceleration above the actuator but a small decelerating force downstream of the powered electrode. This will induce a fluctuation in the temporal evolution of streamwise velocity. This decelerating component needs further investigation as this may inherently limit the performance of a dbd plasma actuator. The computed electron temperature based on the electric field resembles the visible glow that is commonly reported in the literature. For the conical cross-section of a forebody, a large separation occurs due to a 10 m/s at 17.5 deg AOA neutral gas flow past the geometry. A single dbd actuator could not control such separation. Application of seven pulsed dc actuators worked significantly better to control the large vertical structures. In near future we will investigate whether this effect is due to dc Joule heating of the boundary layer (cf. Maslov et al.[15]), electric force or a combination of them.

Acknowledgements

This work was partially supported by the AFOSR grant no. FA9550-05-1-0074 monitored by John Schmisseur and the Air Force Research Laboratory contract no. F33615-98-D-3210 and the National Academy of Science NRC/AFOSR and AFRL research fellowships during the past summers. The authors acknowledge thoughtful discussions with Miguel Visbal.

References

[1] J.P. Bons, R. Sondergard and R.B. Rivir, J. Turbomachinery **123,** 198 (2001). C.L. Enloe, *et al*., AIAA J. **42**, 595 (2004). T.C. Corke and M.L. Post, AIAA-2005-0563, 43rd Aerospace Sciences Meeting, 2005, Reno, Nevada.
[2] J.R. Roth, Phys. Plasmas **10**, 2117 (2003). L.S. Hultgren and D.E. Ashpis, Bull. Amer. Phys. Soc. **47**, No. 10, 167 (2002).
[3] S. Roy, Appl. Phys. Lett. **86**, 101502 (2005). S. Roy and D.V. Gaitonde, AIAA-2005-0160, 43rd Aerospace Sciences Meeting, 2005, Reno, Nevada. S. Roy and D.V. Gaitonde, AIAA-2005-4631, 35th AIAA Fluid Dynamics Conference and 36th AIAA Plasma Dynamics and Lasers Conference, Toronto, Canada, June 2005.
[4] J. R. Roth and X. Dai AIAA-2006-2103, 44th AIAA Aerospace Sciences Meeting and Exhibit, January 9-12, 2006, Reno, Nevada.
[5] S. Roy et al., AIAA-2006-0374, 44th AIAA Aerospace Sciences Meeting and Exhibit, 9-12 Jan 2006, Reno, Nevada. K.P. Singh, S. Roy and D. Gaitonde, Plasma Sources Science and Technology, **15**, 735 (2006).
[6] C. Baird, et al., AIAA-2005-0565, 43rd Aerospace Sciences Meeting, 2005, Reno, Nevada.
[7] W. Shyy, B. Jayaraman and A. Anderson, J. Appl Phys, **92**, 6434 (2002). D.M. Orlov, T.C. Corke and M.P. Patel, AIAA-2006-1202, AIAA 44th Aerospace Sciences Meeting, 2006, Reno, Nevada.
[8] S. Roy and D.V. Gaitonde, J. Appl. Phys. **96**, 2476 (2004). D.V. Gaitonde, M.R. Visbal and S. Roy, AIAA-2005-5302, 36th AIAA Plasmadynamics and laser coferance, June 2005, Toronto, Canada. K.P. Singh and S. Roy, J. Appl. Phys. **98**, 083303 (2005). A.V. Likhanskii et al., AIAA-2006-1204, 44th AIAA Aerospace Sciences Meeting, 2006, Reno, Nevada.

[9] M. Visbal, D. Gaitonde and S. Roy, AIAA-2006-3230, Fluid Dynamics and Flow Control Conference, San Francisco, June 2006. D.V. Gaitonde, M.R. Visbal and S. Roy, AIAA-2006-1205, 44th Aerospace Sciences Meeting, 2006, Reno, Nevada.
[10] G.I. Font, et al. AIAA-2007-188, 45th Aerospace Sciences Meeting and Exhibit, 2007, Reno, Nevada.
[11] K.P. Singh, S. Roy and D. Gaitonde, AIAA-2006-3381, Fluid Dynamics and Flow Control Conference, San Francisco, June 2006.
[12] I. A. Kossyi, A. Yu Kostinsky, A.A. Matveyev and V.P. Silakov, Plasma Sources Sci. Techol., **1**, 207 (1992).
[13] S. Roy and B.P. Pandey, Phys. Plasmas, **9**, 4052 (2002).
[14] H.W. Ellis, et al., Atomic Data Nucl. Data Tables, **17**, 177 (1976).
[15] V. Shalaev, et al., AIAA 2003-34, 41st Aerospace Sciences Meeting and Exhibit, 2003, Reno, Nevada. A. A. Maslov, et al., AIAA-2005-400, 43rd AIAA Aerospace Sciences Meeting and Exhibit 2005, Reno, Nevada.